

## Supplemental Material

**Text.** Expanded methods.

**Table S1.** Infrared stimulated luminescence (IRSL) sample site data, ages, incision rates.

**Figure S1.** Map of infrared stimulated luminescence (IRSL) field sample sites.

**Figure S2.** Field site of IRSL sample 20ABA015-2.

**Figure S3.** Field site of IRSL sample 20ABA017.

**Figure S4.** Field site of IRSL sample 20ABA016.

**Figure S5.** Field site of IRSL sample 20ABA014-4.

**Figure S6.** Field site of IRSL sample 21TOT19.

**Figure S7.** Field site of IRSL sample 21TOT11.

**Figure S8.** Field site of IRSL sample 21TOT18 (omitted from interpretation).

**Figure S9.** Radial plots of IRSL age data.

## Supplemental Materials

### *Rapid active thrust faulting at the northern Alaska Range front*

Adrian Bender<sup>1\*</sup>, Richard O. Lease<sup>1</sup>, Tammy Rittenour<sup>2</sup>, James V. Jones<sup>1</sup>

<sup>1</sup>U.S. Geological Survey Alaska Science Center, Anchorage, Alaska, 99508; \*email: [abender@usgs.gov](mailto:abender@usgs.gov)

<sup>2</sup>Utah State University, Luminescence Lab and Geosciences Department, 1770 North Research Parkway  
Suite 123, North Logan, UT 84341

## DISCLAIMER

Any use of trade, firm, or product names is for descriptive purposes only and does not imply endorsement by the U.S. Government.

## EXPANDED METHODS

### Infrared stimulated luminescence dating

We measured and dated Totatlanika River strath terraces to quantify bedrock incision rates above the Northern Foothills thrust. In the field, we characterized terrace deposits exposed in cutbanks and shallow hand-dug pits at seven sites (Figures S1–S8) that all revealed ~4 m of coarse gravel, similar to the modern bedload, overlying augen and schistose gneiss straths and capped by up to ~1 m of fine–medium sand. We interpreted the sand caps as overbank deposits (cf., Lavé & Avouac, 2000), and used opaque metal pipes to collect infrared stimulated luminescence (IRSL) samples from this unit at each site to date the latest fluvial deposition on the terraces, and thus bracket maximum abandonment and incision onset timing. We analyzed feldspar grains from the seven samples at the Utah State University Luminescence Laboratory following single-aliquot regenerative-dose IRSL (SAR) procedures (Wallinga et al., 2000).

All samples were opened and processed under dim amber safelight conditions within the lab. Sample processing for feldspar IRSL dating followed standard procedures involving sieving, HCl and bleach treatments, heavy mineral separation at  $2.58 \text{ g}\cdot\text{cm}^{-3}$  with no HF pre-treatment, to isolate the potassium-rich feldspar component of a narrow grain-size range, either 75–150 or 150–250  $\mu\text{m}$  as sample material allowed. SAR procedures for potassium feldspar dating involve measuring the IRSL signal 50°C (Wallinga et al. 2000). The SAR protocol includes tests for sensitivity correction and brackets the equivalent dose (DE) the sample received during burial by irradiating the sample at five different doses (below, at, and above the DE, plus a zero dose and a repeated dose to check for recuperation of the signal and sensitivity correction).

The resultant DE data are fit with a saturating exponential curve. The IRSL age is calculated by correcting for fading (loss of signal with time) using the fading method of Auclair et al. (2003) and the age correction model of Huntley and Lamothe (2001). Cumulative DE and age data are reported at  $2\sigma$  and  $1\sigma$  standard error, respectively, and determined using the Central Age Model (CAM) or the Minimum Age Model (MAM) of Galbraith and Roberts (2012). In cases where the samples have significant positive skew, ages were calculated based on a MAM. Dose-rate calculations were determined by chemical analysis of the U, Th, K and Rb content using ICP-MS and ICP-AES techniques by ALS Chemex in Elko, Nevada and conversion factors from Guérin et al. (2011). Internal grain beta dose rate was determined assuming 12.5% K (Huntley and Baril, 1997) and 400ppm Rb (Huntley and Hancock, 2001) attenuated to grain size using Mejdahl (1979). Alpha contribution to dose rate determined using an efficiency factor, ‘a-value’, of  $0.09\pm 0.01$  after Rees-Jones (1995). The contribution of cosmic radiation to the dose rate was calculated using sample depth, elevation, and latitude/longitude following Prescott and Hutton (1994). Dose rates are calculated based on water content, sediment chemistry, and cosmic contribution (Aitken and Xie, 1990; Aitken, 1998).

From the fade-corrected dose rate and single-aliquot age data (Auclair et al., 2003; Huntley & Lamothe, 2001), we computed six central age models (CAM), as well as one minimum age model (MAM) for one sample with strongly positive-skewed aliquot ages (Galbraith & Roberts, 2012). IRSL ages of  $4.4\pm 0.8 \text{ ka}$  (MAM),  $6.0\pm 0.8 \text{ ka}$ ,  $7.3\pm 0.7 \text{ ka}$ ,  $9.8\pm 0.9 \text{ ka}$ ,  $38.3\pm 5.6 \text{ ka}$ , and  $65.8\pm 6.4 \text{ ka}$  bound the onset timing of incision equal to strath height above the active channel, measured via TruPulse 200L laser range finder in the field (Table S1; Figures S1–S7). We omit the CAM result for sample 21ABA18, collected in the synclinal topographic low south of the Rex anticline. Sample 21ABA018 yielded an age of  $4.2\pm 0.4 \text{ ka}$  for a sand horizon capping a strath 14 m above the active channel (Figure S8); the implicit incision rate of ~3.3 mm/yr exceeds two nearby incision rates (~0.4 mm/yr at 21ABA19; ~0.7 mm/yr at 21ABA11) by at least a factor of four to seven without structural changes to account for an uptick in incision rate. Rather than interpret this anomalously fast incision rate (and young age), we attribute the result to post-depositional sediment mixing by roots observed in the field (Figure S8). Unfortunately, the only accessible exposures of the sand mantle at this location contained abundant medium–fine and

common coarse roots. Bioturbation associated with such rooting can translocate more recently sun-exposed mineral grains to depth and thus impose artificially young IRSL ages (e.g., Hanson et al., 2015).

### **Modeling the Northern Foothills thrust from kinematic constraints**

We assumed that our Totatlanika River incision rates, computed from IRSL ages of terrace alluvium and field measurements of terrace strath height, delimit the pace of rock uplift on the Northern Foothills thrust. Consistent with contemporary near-zero post-glacial isostatic adjustment (GIA) across the study area (Vishwakarma et al., 2022), we assume negligible millennial scale GIA influence on the measured incision rates, which spatially covary with mapped structures and topography expected to produce and result from differential rock uplift, respectively. Treating the rates of fluvial downcutting as kinematic constraints on rock uplift, a fault accommodating known north-directed Northern Foothills thrust geometry should be quantitatively related to the hanging wall velocity (Hardy & Poblet, 2005). To quantify the contemporary (horizontal) hanging wall velocity, we computed the Northern Foothills thrust-normal (N8.5°W at the longitude of study) GPS velocities from the velocity solutions of Elliott & Freymueller (2020).

We calculated the velocity gradient across the Northern Foothills thrust as the difference between the average of five clustered velocities south of the fault trace ( $4.84 \pm 0.08$  mm/yr) but north of the central Denali Fault and the velocity ~20 km north of the fault trace at station NENA ( $0.48 \pm 1.27$  mm/yr). This analysis omitted two velocities that plot well outside the average and uncertainty of clustered hanging wall velocities (Figure 3a). The resulting  $4.36 \pm 2.10$  mm/yr velocity gradient accounts for ~78% of the 5.6 mm/yr geologic residual Yakutat microplate velocity along the central Denali Fault. All GPS velocity solutions used in this analysis were published in Elliott & Freymueller (2020) and are provided in the EF20\_GPSvelocity tab of a supplemental Excel file. We used the GPS velocity gradient ( $h$ ) across the Northern Foothills thrust as the horizontal hanging wall velocity, and imposed this velocity on a trishear fault-propagation fold model (Hardy & Poblet, 2005). This approach assumes that the Northern Foothills thrust, which is the most prominent active fault mapped in the ~70 km N-S distance that the geodetic gradient spans (Elliott & Freymueller, 2020; Bemis & Wallace, 2007), takes up all the contemporary velocity.

We used the method of Hardy and Poblet (2005) to ascertain fault geometry at depth based on hanging wall velocities for a trishear fault-propagation fold. This approach relates slip rate ( $s$ ), horizontal rock velocity ( $u$ ), vertical rock velocity ( $v$ ), and fault dip ( $\delta$ ). Above the detachment domain, the equations are:

$$u = s \cos(\delta_1) \quad (1)$$

$$v = s \sin(\delta_1) \quad (2)$$

where  $\delta_1$  indicates detachment dip. Above the ramp domain, the equations are:

$$u = R_0 s \cos(\delta_2) \quad (3)$$

$$v = R_0 s \sin(\delta_2) \quad (4)$$

where  $\delta_2$  indicates ramp dip. The slip ratio  $R_0$  accounts for the change in slip between the detachment and ramp, and is computed as:

$$R_0 = \sin(\gamma + \delta_1) / \sin(\gamma + \delta_2) \quad (5)$$

where the dip of the active back-axial surface is determined as  $\gamma = (180 - \delta_2)/2$ .

We assume that the fastest two incision rates measured nearest the range front (4.78 mm/yr and 5.64 mm/yr; average = 5.21 mm/yr) reflect the vertical velocity above the ramp. Upstream and to the south, we assume that the intermediate incision rate of 1.1 mm/yr occurs across the axial surface between



the ramp and detachment, and the remaining 3 incision rates to the south of the Rex anticline (average 0.55 mm/yr) occur above the detachment.

We first used Equation 1 with  $h = u$  and Equation 2 with  $v = 0.55$  mm/yr to set detachment dip by numerically solving  $\delta_1 = 1\text{--}10^\circ$ . By this approach,  $\delta_1 = 7^\circ$  south for both velocity components produced mutually compatible slip rate solutions equivalent to the GPS convergence rate  $h$ , explicitly assuming that long-term slip on a low-angle detachment matches short-term hanging wall surface velocity. We then numerically solved Equations 4 and 5 for  $\delta_2 = 44\text{--}52^\circ$ , with  $s$  solved as  $v/R_0\sin(\delta_2)$  for each iteration. We selected the steep ramp angle range to reflect measured incision rates that exceed the geodetic shortening rate. This approach produced ranges of  $v$  that narrowed plausible slip rates for each ramp dip to 5–7 mm/yr, for which we repeated the numerical approach with slip rate increments of 0.1 mm/yr. This second iteration converged on  $v = 5.21$  mm/yr (equal to the average assumed ramp incision rates) with  $\delta_2 = 48^\circ$  south and  $s = 6.7$  mm/yr. We acknowledge that multiple dip and slip rate combinations may produce compatible rock uplift rates, however, the range of dips tested with  $s = 6.7$  mm/yr closely match the observed range of ramp incision rates and bolster confidence in the ramp dip solution of  $\delta_2 = 48 \pm 4^\circ$  (1 $\sigma$  uncertainty reflects the range of ramp dips tested). We arbitrarily assign a ~25% 1 $\sigma$  uncertainty to the ramp (6.4 mm/yr) and detachment (4.4 mm/yr) slip rates and rock uplift rates obtained by this approach.

We defined the trishear zone and fault depths based on the observed incision rate field and the topographic expression of the Rex anticline. Horizontal and vertical rock velocities are expected to vary continuously with depth across the trishear zone at the fault tip, from equal to the hanging wall velocity at the top to equal to the fixed footwall velocity at the base, explicitly assumed to be zero (e.g., Hardy & Allmendinger, 2011; Hardy & Poblet, 2005). Our assumed hanging wall incision rates may therefore occur in the top of the trishear zone. The forelimb hinge commonly marks the upper trishear zone boundary, however, and occurs on the Rex anticline at a distance between the two ramp incision rate observations in profile space. Hence, we place the top trishear zone boundary at a profile distance  $x = 21.8$  km, between the two ramp incision rate observations and consistent with the apparent hinge position in the topographic swath profile. We follow common trishear zone conventions of symmetry about the fault tip with an apical angle set to  $60^\circ$  (Hardy & Allmendinger, 2011). Given the steep  $48^\circ$  ramp dip, we assume a vertical boundary between the hanging wall and trishear domains, and fix the lower trishear boundary at the range front at  $x = 18.0$  km just north of an apparent footwall syncline (e.g., Fig. 3 of Hardy & Allmendinger, 2011; Erslev, 1991). This configuration places the Northern Foothills thrust ramp tip at a depth of 1.9 km beneath the surface, set to the river channel elevation  $y = 0.28$  km at profile distance  $x = 21.8$  km, 3.8 km south of the stable footwall just north of the range front.

We determined the coordinates of the intersection of the ramp, detachment, and active back-axial surface (24.2 km distance, 4.6 km depth) graphically as the intersection of representative lines. The ramp line dips in the positive profile direction from the fault tip coordinate (21.8 km distance, 1.9 km depth) at  $48^\circ$ . The active back-axial surface line dips in the negative profile direction at  $66^\circ$  from the surface elevation of the river (26.5 km distance, 0.4 km elevation) where we measure a 1.1 mm/yr incision rate and assume the back-axial surface intersects the Earth surface. We allow modeled rock uplift rates to vary continuously from the down-dip edge of the ramp domain (24.2 km distance, 5.2 mm/yr) to down-dip of the subaerial projection of the back-axial surface above the detachment domain (26.8 km distance, 0.6 mm/yr) such that the modeled rock uplift rate intersects the 1.1 mm/yr measured at site 20ABA014-4 (Figs. S 1, S5). The detachment dips  $7^\circ$  south from the base of the ramp (24.2 km distance, 4.6 km depth) toward the Denali Fault, effectively infinitely for our purposes, and intersects the 1947 M7.1 earthquake hypocenter depth of  $6 \pm 4$  km (Fletcher & Christensen, 1996) at 38.5 km distance and 5.7 km depth. Both our modeled fault and the hypocenter depth of Fletcher & Christensen (1996) occur far above the  $26 \pm 5$  km-deep 1947 hypocenter of Bondár and others (2015), which places the source at sub-Moho depth (Miller et al., 2018). We contend that the strong shaking of  $\text{MMI} \leq 8$  reported on and tens of kilometers north of the Northern Foothills thrust hanging wall (St. Amand, 1948) are inconsistent with the sub-Moho source depth of Bondár and others (2015), but are compatible with the shallow north-vergent thrust sources implied by (1) our model, (2) the hypocenter depth of Fletcher & Christensen (1996), and (3) the structural cross section of Bemis & Wallace (2007).

### Sources of uncertainty in prior estimates of Northern Foothills thrust rates

We report rates of convergence ( $4.4 \pm 2.1$  mm/yr; geodetic) on the Northern Foothills thrust that inform a model of thrust slip ( $4.4\text{--}6.7$  mm/yr) and rock uplift (up to  $5.2 \pm 1.3$  mm/yr) constrained by measured bedrock incision rates. Our results at least double the  $0.4\text{--}2.3$  mm/yr total shortening and related rates reported by Bemis et al. (2015) with reference to Bemis (2010). To accompany the description of our approach and related sources of uncertainty detailed above and in the paper that this document supplements, here we summarize the lineage of the prior rate range and consider potential sources of uncertainty that likely contributed to the low estimate.

#### Summary of Bemis (2010) and Bemis (2015) rate estimates

Bemis (2010) derived slip rates from elevation profiles and inferred ages of faulted landforms, including glaciofluvial terraces and panels underlain by Pliocene-Pleistocene Nenana Gravel, along the Nenana and Teklanika/Savage Rivers, which drain the Alaska Range  $\sim 20\text{--}30$  km west of our Totatlanika River study area [Figure 3.3 of Bemis (2010)]. Elevation profiles are based on digital elevation models or field survey data with maximum quoted uncertainty of 5 m and an additional  $\sim 5$  m of reported surface elevation variability (Bemis, 2010). A combination of Marine Isotope Stage ages and tentative correlations between the terraces and glacial advances of coarsely constrained age from prior independent studies inform the timing of terrace and landform formation and thus provide speculative ages of landform abandonment (see Table 3.1 of Bemis (2010)). Bemis (2010) measured vertical offsets in several of the terrace and Nenana Gravel surfaces across the Northern Foothills thrust and a backthrust termed the Stampede fault (see Table 3.1 of Bemis (2010)). Assigning dips to each fault thought plausible based on the terrace elevation profiles [Table 3.2 of Bemis (2010) and Figure 3.7 of Bemis (2010)], Bemis (2010) calculated slip rates for each fault that range from  $0.25\text{--}1.00$  mm/yr based on the measured offsets and speculative surface ages [Figure 3.9 of Bemis (2010)]. Concluding this analysis, Bemis (2010) quoted a shortening rate:

*“The previous chapter uses the sequence of fluvial terraces along Nenana River valley as structural markers to constrain the structural geometry and rate of deformation across this portion of the northern Alaska Range fold-thrust belt. Converting the slip rates of these individual faults into a horizontal shortening rate across the system, and allowing for generous uncertainties, suggests that  $1\text{--}3$  mm/yr of shortening is accommodated within the Alaska Range north of the Denali fault.”*

The quoted shortening rate is presented in Bemis et al. (2015) as both  $1\text{--}3$  mm/yr (e.g., their Figure 3) and as  $0.4\text{--}2.3$  mm/yr (e.g., their Table 2). We acknowledge that the results of Bemis (2010) represent the best effort with limited available data. However, the approach of Bemis (2010) and Bemis et al. (2015) introduce both aleatoric and epistemic uncertainty to the quoted rates through the fault model and the correlative offset landform ages that underpin their results. Aleatoric uncertainty represents random error inherent in a dataset that contributes to quantifiable uncertainty, while epistemic uncertainty represents error introduced to a model or interpretation by low data quality or quantity, and/or omission of factors that may influence a model result. Below, we consider uncertainties in the fault model and correlative ages that the rates reported by Bemis (2010) and Bemis et al. (2015) rely on.

#### Fault model uncertainties

The fault model of Bemis (2010) comprises a planar south-dipping ( $20 \pm 5^\circ$ ; Table S4) Northern Foothills thrust and a north-dipping ( $28 \pm 7^\circ$ ; Table S4) listric back-thrust termed the Stampede fault. This fault configuration results from an interpretation of landform elevation profiles across the fault traces that

involved reasoning out other fault models deemed unlikely to produce systematic landform surface steepening to the north as Bemis (2010) observed on the Stampede fault hanging wall. Prior studies (e.g., Briner & Kaufman, 2008; Ritter, 1982; Ritter & Ten Brink, 1986; Wahrhaftig & Black, 1958) describe the same landforms (excluding Pliocene-Pleistocene basin-fill of the Nenana Gravel) as a complex sequence of outwash terraces mantled by glaciofluvial, fan, and/or aeolian deposits collectively up to 47 m thick (Ritter, 1982). Several of these studies' interpretations differ from Bemis (2010) in that they ascribe north-sloping terrace elevation profiles primarily to northward (downstream) thinning of the glacial outwash and related deposits (e.g., Wahrhaftig & Black, 1958; Ritter, 1982; Ritter & Ten Brink, 1986). Similarly, the ancient basin-fill Nenana Gravel (Tn) thickness is thought to decrease from 1000 to 500 m northward across the Stampede fault (Thoms, 2000).

The landform elevation profiles likely reflect some combination of deposit thickness variability and post- and/or syn-depositional differential uplift, but the unknown magnitude of either factor introduces epistemic uncertainty to the fault model and offset magnitudes of Bemis (2010). Bemis (2010) apparently measured vertical offsets between discontinuously mapped landforms (e.g., Tn, Q2) separated by kilometers across the Northern Foothills thrust and the Stampede fault and across a broad region spanning  $\leq 20$  km east–west. The thickness of deposits underlying these landforms is known to vary by tens to hundreds of meters, and both the Nenana Gravel and the glaciofluvial deposits are expected to systematically thin downstream (e.g., Ritter, 1982; Thoms, 2000). Given the apparent several kilometer downstream span ( $\leq 10$  km?) between measured hanging wall and foot wall landform elevations, it remains unclear how much of the fault offset measured by Bemis (2010) may be masked by systematic northward/downstream deposit thinning. For example, thinning of the Nenana Gravel by  $\sim 500$  m north across the Stampede fault (Thoms, 2000) reflects 25% of the 2000 m fault-parallel Nenana Gravel offset that Bemis (2010) reports, and could therefore lead to an underestimate of the fault offset and thus contribute to rate underestimation.

#### Landform age uncertainties

Ages that constrain slip and shortening rates reported by Bemis (2010) and Bemis et al. (2015) reflect tentative correlations between faulted glaciofluvial terraces and surfaces underlain by Nenana Gravel, and the poorly constrained timing of several regional glacial advances. None of the measured offset surfaces were directly dated [Table 3.1 of Bemis (2010)]. Age correlations for faulted landforms listed therein reference Marine Isotope Stages and the tentative correlations of previous researchers who traced glaciofluvial terrace tread elevations to moraines hypothesized to represent the glacial source for the landforms. Briner and Kaufman (2008) summarized the limited reliable age data available at the time of Bemis (2010) to test or refine the timing of glaciations  $\leq 60$  ka. Older glacial landforms were not directly dated at the time, leaving the Quaternary-spanning correlative chronology of Bemis (2010) largely untested. Given that the measured terraces and the latest Cenozoic Nenana Gravel undoubtedly represent time-transgressive depositional surfaces, a single tentative age of formation cannot robustly bracket either the timing of formation or abandonment attributed to fault-driven rock uplift. Therefore, the aleatoric uncertainty of each glaciation age (e.g., Marine Isotope Stage bounds) bears uncertain meaning for either the timing of glaciation or the timing of related paraglacial processes such as glaciofluvial terrace formation. Further removed from these correlative landform ages is the timing of surface-breaking faulting. For example, available evidence implies deposition of the ancient basin-filling Nenana Gravel between 4.5 and 1 Ma (Athey et al., 2006; Nørgaard et al., 2023), effectively leaving a 4.5 million year-long time interval during which faulting of the unit may have occurred. Hence, the rates resulting from the correlations of Bemis (2010) contain prominent but unquantifiable epistemic uncertainty in that it is unclear what relationship the assigned ages bear to either landform formation or hypothesized abandonment via faulting.

### Record completeness

Another factor that may contribute uncertainty to the rate estimates of Bemis (2010) is the potential incompleteness of fault rate records they summed across the range ~20–30 km west of our Totatlanika River study area. For example, Federschmidt (2014) identified evidence for 0.6–1.2 mm/yr of slip in the last ~2 kyr in trenches excavated across a fault that they referred to as the Hines Creek fault in keeping with previous mapping, but may be kinematically related to the suspected active Park Road fault. Federschmidt (2014) characterized the fault as a steeply ( $84^{\circ}$ – $88^{\circ}$ ) north-dipping back-thrust. These slip rate and fault dip ranges imply shortening rates up to 0.1 mm/yr across the fault, and so negligibly contribute to the total shortening rate across the range. However, if the fault dip decreases at depth to, for example,  $45^{\circ}$  north, the higher end of the 2 kyr-spanning slip rate range may accommodate ~0.8 mm/yr shortening which would add substantially to the quoted 1–3 mm/yr total shortening at equivalent longitude (Bemis, 2010). Given substantial uncertainty regarding the geometry and longer-term late Pleistocene deformation rates across the Park Road fault, however, we view the omission of this fault rate as a comparatively marginal source of uncertainty contributing to the low total shortening rate estimated by Bemis (2010).

## DATA AVAILABILITY

### Independently published data used in this study

Field measurements and IRSL data that support this study are available through the U.S. Geological Survey Alaska Science Center Science Portal at <https://doi.org/10.5066/P96KN145>. The general bathymetric chart of the oceans (GEBCO) grayscale rendering ([https://www.gebco.net/data\\_and\\_products/gridded\\_bathymetry\\_data/gebco\\_2021/](https://www.gebco.net/data_and_products/gridded_bathymetry_data/gebco_2021/), last access: 24 October 2022) provides the base map for Figure 1. The Alaska IfSAR digital elevation model, used in Figure 2 (map renderings), Figure 3 (elevation profiles), and Figure S1 (map rendering) is available for download from (1) the U.S. Geological Survey by searching <https://earthexplorer.usgs.gov/>, and (2) the Alaska Department of Geological and Geophysical Surveys by searching <https://elevation.alaska.gov/>.

### Supplemental data published with this study

The supplement to this paper includes a Microsoft Excel file with the following content:

- Tab “DFs\_RateData” – includes published Denali Fault slip rate site locations, ages, measured offsets, and sources used and cited in this study.
- Tab “DFs\_RateResidualSections” – includes Denali Fault section average rates, rate regression parameters, and Yakutat residual velocities calculated in this study.
- Tab “1947MMI” – contains Modified Mercalli Intensity estimates and locations for the 1947 M7.1 Healy Earthquake plotted in St. Amand (1948) and published in Brockman et al. (1988).
- Tab “1947epicenter” – contains location information for the 1947 Healy Earthquake mainshock and aftershock sourced in the ISC-GEM catalog (Bondár et al., 2015).
- Tab “EF20\_GPSvelocity” contains GPS velocity solutions and locations from Elliott & Freymueller (2020) used in this study, as well as Northern Foothills thrust-normal velocities calculated in this study.
- Tab “TotatlanikaRiverProfile” – contains profile distance (swath profile in Figures 2 and 3), latitude, longitude, elevation, and drainage area for Totatlanika River pixels as delineated on the Alaska IfSAR DEM using codes of Forte & Whipple (2019) and Schwanghart & Scherler (2014) in MATLAB 2017b, and extracted by standard procedures in ArcMap 10.8.
- Tab “IRSL\_AgeData” – contains infrared stimulated luminescence age data from the Utah State University lab report from this study, also available in Bender (2022).
- Tab “IRSL\_DoseRateData” – contains infrared stimulated luminescence (IRSL) dose rate data from the Utah State University lab report from this study, also available in Bender (2022).
- Tab “IRSL\_SiteAgeRateData” – contains sample location information, IRSL ages, measured strath height, and calculated incision rates from this study, also available in Bender (2022).
- Tab “tiltProfiles” – contains data for elevation profiles extracted from the Alaska IfSAR DEM across the 7.3 ka Totatlanika River terrace and the tilted Nenana Gravel at the northern Alaska Range front, plotted in Figure 3d.
- Tab “NFt\_HardyPoblet2005” – contains velocity-based trishear fault-propagation fold model based on the approach of Hardy and Poblet (2005).

## REFERENCES

- Aitken, M.J. 1998: An Introduction to Optical Dating: The dating of Quaternary sediments by the use of photon-stimulated luminescence. New York, Oxford University Press, 267 p.
- Aitken, M.J., Xie, J., 1990. Moisture correction for annual gamma dose. *Ancient TL* 8 (2), 6-9.
- Amos, C.B., Burbank, D.W., Nobes, D.C. and Read, S.A., 2007. Geomorphic constraints on listric thrust faulting: Implications for active deformation in the Mackenzie Basin, South Island, New Zealand. *Journal of Geophysical Research: Solid Earth*, 112(B3).
- Athey, J., Newberry, R., Werden, M., Freeman, L., Smith, R., & Szumigala, D. (2006). Bedrock geologic map of the Liberty Bell area, Fairbanks A-4 Quadrangle, Bonfield mining district, Alaska. In *Alaska Division of Geological & Geophysical Surveys Report of Investigation RI2006: Vol. 1.0.1*. <https://doi.org/https://doi.org/10.14509/15026>
- Auclair, M., Lamothe, M., Huot, S., 2003. Measurement of anomalous fading for feldspar IRSL using SAR. *Radiation Measurements* 37, 487-492.
- Bender, A. M., 2022, Totatlanika River terrace luminescence age data collected 2020-2022: U.S. Geological Survey data release, <https://doi.org/10.5066/P96KN145>.
- Bemis, S.P., 2010. Moletrack Scarps to Mountains: Quaternary Tectonics of the Central Alaska Range [Ph. D. thesis]: Eugene. *Oregon, University of Oregon*. [https://scholarsbank.uoregon.edu/xmlui/bitstream/handle/1794/10563/Bemis\\_Sean\\_Patrick\\_phd2010win.pdf](https://scholarsbank.uoregon.edu/xmlui/bitstream/handle/1794/10563/Bemis_Sean_Patrick_phd2010win.pdf)
- Bemis, S. P., & Wallace, W. K. (2007). Neotectonic framework of the north-central Alaska Range foothills. *The Geological Society of America Special Paper* 431, 2431(21), 549–572. [https://doi.org/10.1130/2007.2431\(21\)](https://doi.org/10.1130/2007.2431(21)).
- Bemis, S. P., Weldon, R. J., & Carver, G. A. (2015). Slip partitioning along a continuously curved fault: Quaternary geologic controls on Denali fault system slip partitioning, growth of the Alaska Range, and the tectonics of south-central Alaska. *Lithosphere*, 3, 235–246. <https://doi.org/10.1130/L352.1>
- Bondár, I., Engdahl, E. R., Villaseñor, A., Harris, J., & Storchak, D. (2015). ISC-GEM: Global Instrumental Earthquake Catalogue (1900-2009), II. Location and seismicity patterns. *Physics of the Earth and Planetary Interiors*, 239, 2–13. <https://doi.org/10.1016/j.pepi.2014.06.002>
- Briner, J. P., & Kaufman, D. S. (2008). Late Pleistocene mountain glaciation in Alaska: key chronologies. *Journal of Quaternary Science*, 23, 659–670. <https://doi.org/10.1002/jqs>
- Dortch, J. M., Owen, L. A., Caffee, M. W., Li, D., & Lowell, T. V. (2010). Beryllium-10 surface exposure dating of glacial successions in the Central Alaska Range. *Journal of Quaternary Science*, 25(8), 1259–1269. <https://doi.org/10.1002/jqs.1406>
- Elliott, J. L., & Freymueller, J. T. (2020). A Block Model of Present - Day Kinematics of Alaska and Western Canada *Journal of Geophysical Research : Solid Earth. Journal of Geophysical Research*, 1–30. <https://doi.org/10.1029/2019JB018378>
- Erslev, E. A. (1991). Trishear fault-propagation folding. *Geology*, June, 617–620. [https://doi.org/doi.org/10.1130/0091-7613\(1991\)019<0617:TFPF>2.3.CO;2](https://doi.org/doi.org/10.1130/0091-7613(1991)019<0617:TFPF>2.3.CO;2)
- Fletcher, H. J., & Christensen, D. H. (1996). A Determination of Source Properties of Large Intraplate Earthquakes in Alaska. *Pure and Applied Geophysics*, 146(1), 21–41. <https://doi.org/https://doi.org/10.1007/BF00876668>
- Hardy, S., & Allmendinger, R. W. (2011). Trishear: A review of kinematics, mechanics, and applications. *AAPG Memoir*, 94, 95–119. <https://doi.org/10.1306/13251334M943429>
- Hardy, S., & Poblet, J. (2005). A method for relating fault geometry, slip rate and uplift data above fault-propagation folds. *Basin Research*, 17, 417–424. <https://doi.org/10.1111/j.1365-2117.2005.00268.x>
- Kaufman, D. S., Young, N. E., Briner, J. P., & Manley, W. F. (2011). Alaska Palaeo-Glacier Atlas (Version 2). *Developments in Quaternary Science*, 15 (Version 2), 427–445. <https://doi.org/10.1016/B978-0-444-53447-7.00033-7>
- Miller, M. S., Driscoll, L. J. O., Porritt, R. W., & Roeske, S. M. (2018). Multiscale crustal architecture of Alaska inferred from P receiver functions. *Lithosphere*, 10(2), 267–278. <https://doi.org/https://doi.org/10.1130/L701.1>
- Nørgaard, J., Jansen, J. D., Neuhuber, S., & Knudsen, M. F. (2023). P – PINI : A cosmogenic nuclide

- burial dating method for landscapes undergoing non-steady erosion. *Quaternary Geochronology*, 74. <https://doi.org/10.1016/j.quageo.2022.101420>
- Ritter, D. F. (1982). Complex river terrace development in the Nenana Valley near Healy, Alaska. *Geological Society of America Bulletin*, 93(4), 346–356. [https://doi.org/10.1130/0016-7606\(1982\)93<346:CRTDIT>2.0.CO;2](https://doi.org/10.1130/0016-7606(1982)93<346:CRTDIT>2.0.CO;2)
- Ritter, D. F., & Ten Brink, N. W. (1986). Alluvial fan development and the glacial-glaciofluvial cycle, Nenana Valley, Alaska. *Journal of Geology*, 94(4), 613–625. <https://doi.org/10.1086/629063>
- St. Amand, P. (1948). The Central Alaska Earthquake Swarm of October 1947. *Transactions, American Geophysical Union*, 29(5). <https://doi.org/doi/pdf/10.1029/TR029i005p00613>
- Vishwakarma, B. D., Ziegler, Y., Bamber, J. L., & Royston, S. (2022). Separating GIA signal from surface mass change using GPS and GRACE data. *Geophysical Journal International*, 232(1), 537–547. <https://doi.org/10.1093/gji/ggac336>
- Wallinga, J., Murray, A., Wintle, A., 2000. The single-aliquot regenerative-dose (SAR) protocol applied to coarse-grain feldspar. *Radiation Measurements* 32, 529-533.

## **TABLES AND FIGURES**

Table S1: Infrared stimulated luminescence (IRSL) sample site data, ages, incision rates.

Figure S1: Map of infrared stimulated luminescence (IRSL) field sample sites.

Figure S2: Field site of IRSL sample 20ABA015-2.

Figure S3: Field site of IRSL sample 20ABA017.

Figure S4: Field site of IRSL sample 20ABA016.

Figure S5: Field site of IRSL sample 20ABA014-4.

Figure S6: Field site of IRSL sample 21TOT19.

Figure S7: Field site of IRSL sample 21TOT11.

Figure S8: Field site of IRSL sample 21TOT18 (omitted from interpretation).

Figure S9: Radial plots of IRSL age data.



**Table S1:** Infrared stimulated luminescence (IRSL) sample site data, ages, incision rates.<sup>1</sup>

Sample ID	Lat.*	Long.*	Elevation (m)**	Sample depth (m)***	Tread height (m)****	Strath height (m)****	IRSL age (ka)	IRSL age 1 $\sigma$ (ka)	Incision rate (m/kyr)	Incision rate 1 $\sigma$ (m/kyr)
20ABA0 15-2	64.2058	-148.7658	309.8	1.75	40	35	7.32	0.68	4.78	0.81
20ABA0 17	64.1868	-148.7441	356.1	0.35	60	55	9.76	0.87	5.64	0.72
20ABA0 16 <sup>+</sup>	64.1625	-148.6851	391.2	0.75	4	0	4.36	0.79	0.00	1.15
20ABA0 14-4	64.1597	-148.6925	456.0	0.60	75	70	65.80	6.37	1.06	0.13
21TOT1 9	64.1155	-148.5418	523.1	0.95	20	16	38.29	5.60	0.42	0.14
21TOT1 1	64.1002	-148.5051	544.9	0.85	7	4	6.00	0.78	0.67	0.84

<sup>1</sup>Additional IRSL age data and parameters reported in the supplemental Microsoft Excel file and Bender (2022).

\* NAD83 latitude and longitude in decimal degrees.

\*\*Elevation extracted from the 5 m-resolution Alaska IfSAR digital elevation model.

\*\*\*Depth of center of IRSL sample measured from terrace tread.

\*\*\*\*Heights measured via laser range finder and relative to modern channel near water level.

<sup>+</sup>Minimum age model due to significant positive skew, otherwise central age model (Galbraith and Roberts, 2012).

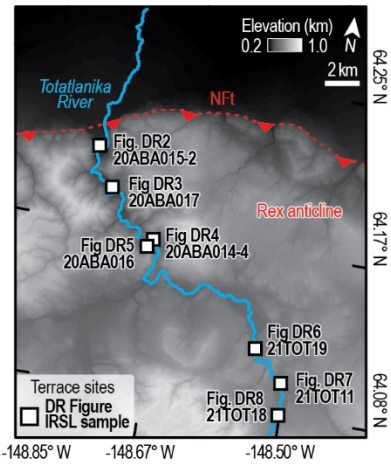


Figure S1: Map of IRSL (infrared stimulated luminescence) sample sites and S (data repository) figures. Northern Foothills thrust—NFT.

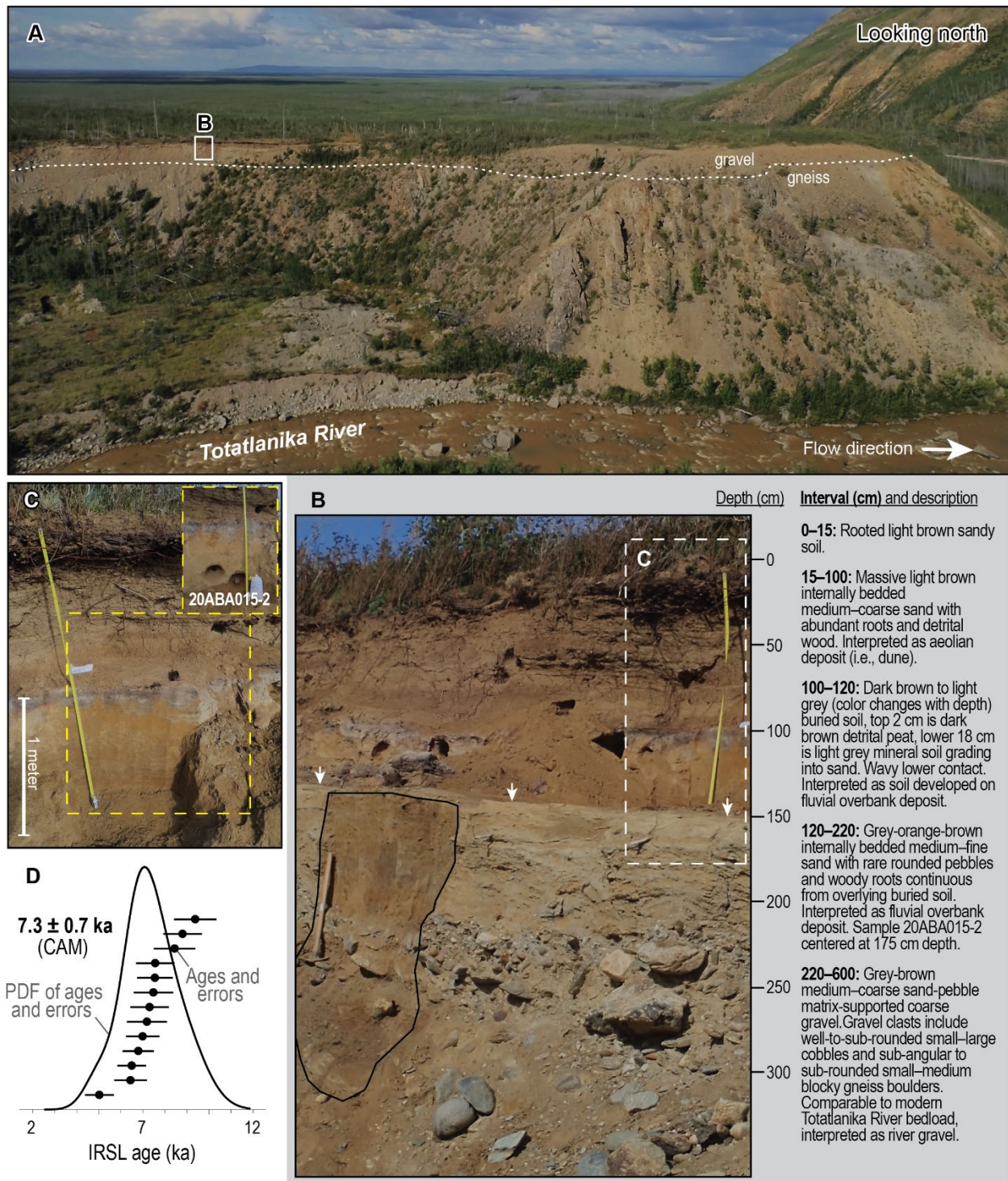


Figure S2: Field site of infrared stimulated luminescence (IRSL) sample 20ABA015-2. (A) Site overview, white dashed line marks strath, white box marks (B) Sample exposure and description. White arrows mark bench excavated into sand horizon, likely recently by prospectors but prior to our site occupation. Black polygon outlines cleaned and described lower section. White dashed box marks (C) sample horizon detail. (D) IRSL ages, probability distribution, and central age model result (CAM; Galbraith & Roberts, 2012) of sample 20ABA015-2.



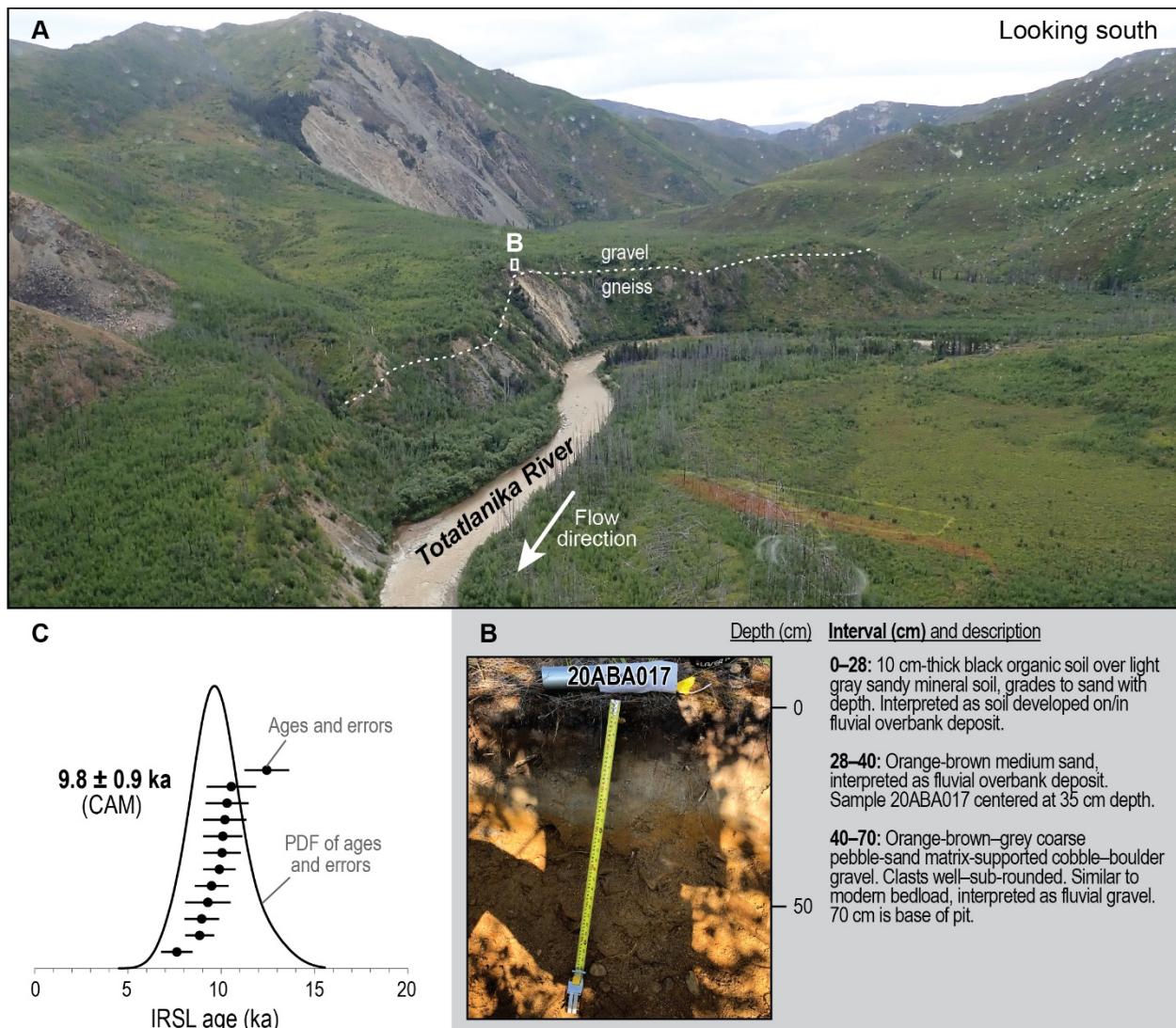


Figure S3: Field site of infrared stimulated luminescence (IRSL) sample 20ABA017. (A) Site overview, white dashed line marks strath, white box marks (B) sample exposure and description. (C) IRSL ages, probability distribution, and central age model result (CAM; Galbraith & Roberts, 2012) of sample 20ABA017.

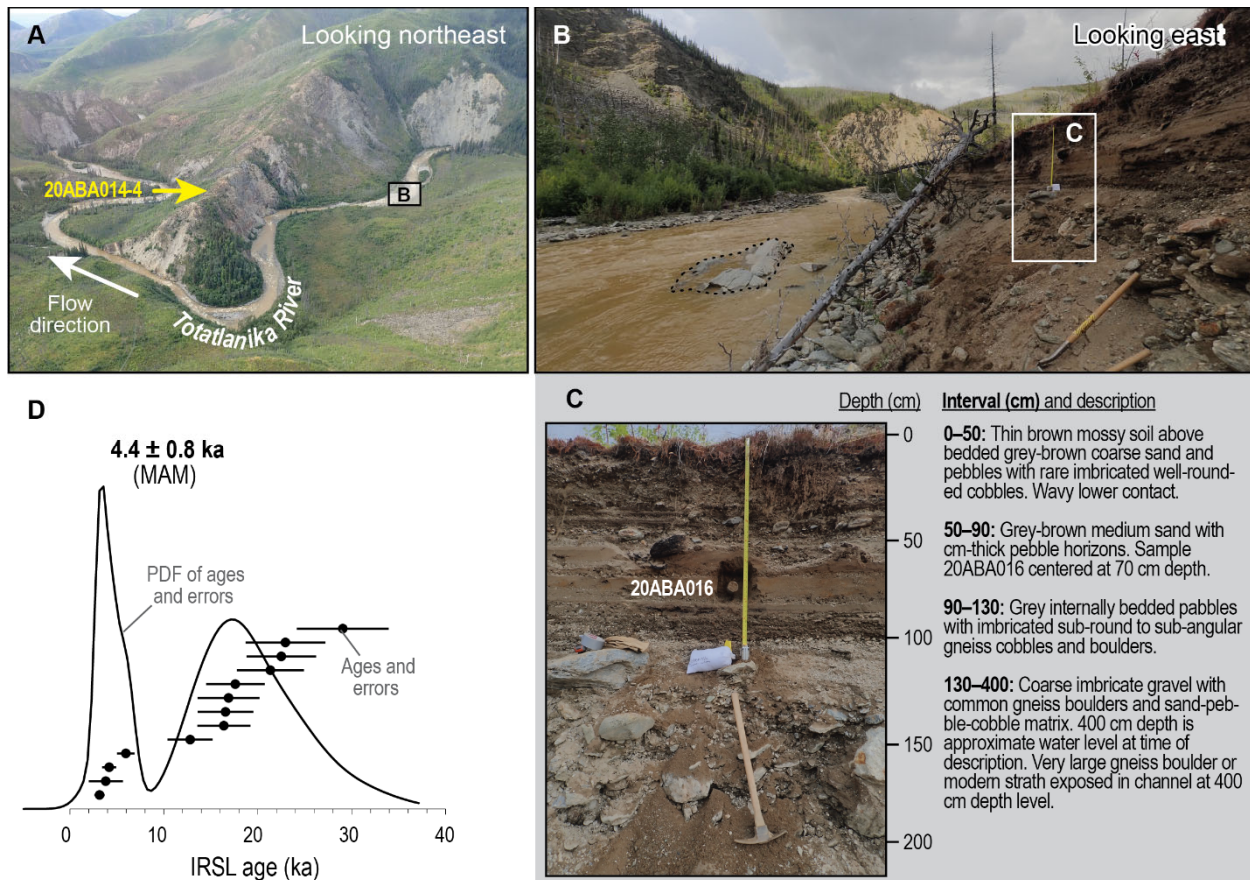


Figure S4: Field site of infrared stimulated luminescence (IRSL) sample 20ABA016. (A) Site overview, yellow arrow marks site 20ABA014 characterized in Figure S5. Black box marks (B) deposit exposure, black dashed polygon outlines large gneiss boulder or strath at water level, white box marks (C) sampled section and description. (D) IRSL ages, probability distribution, and minimum age model result (MAM; Galbraith & Roberts, 2012) of sample 20ABA016.



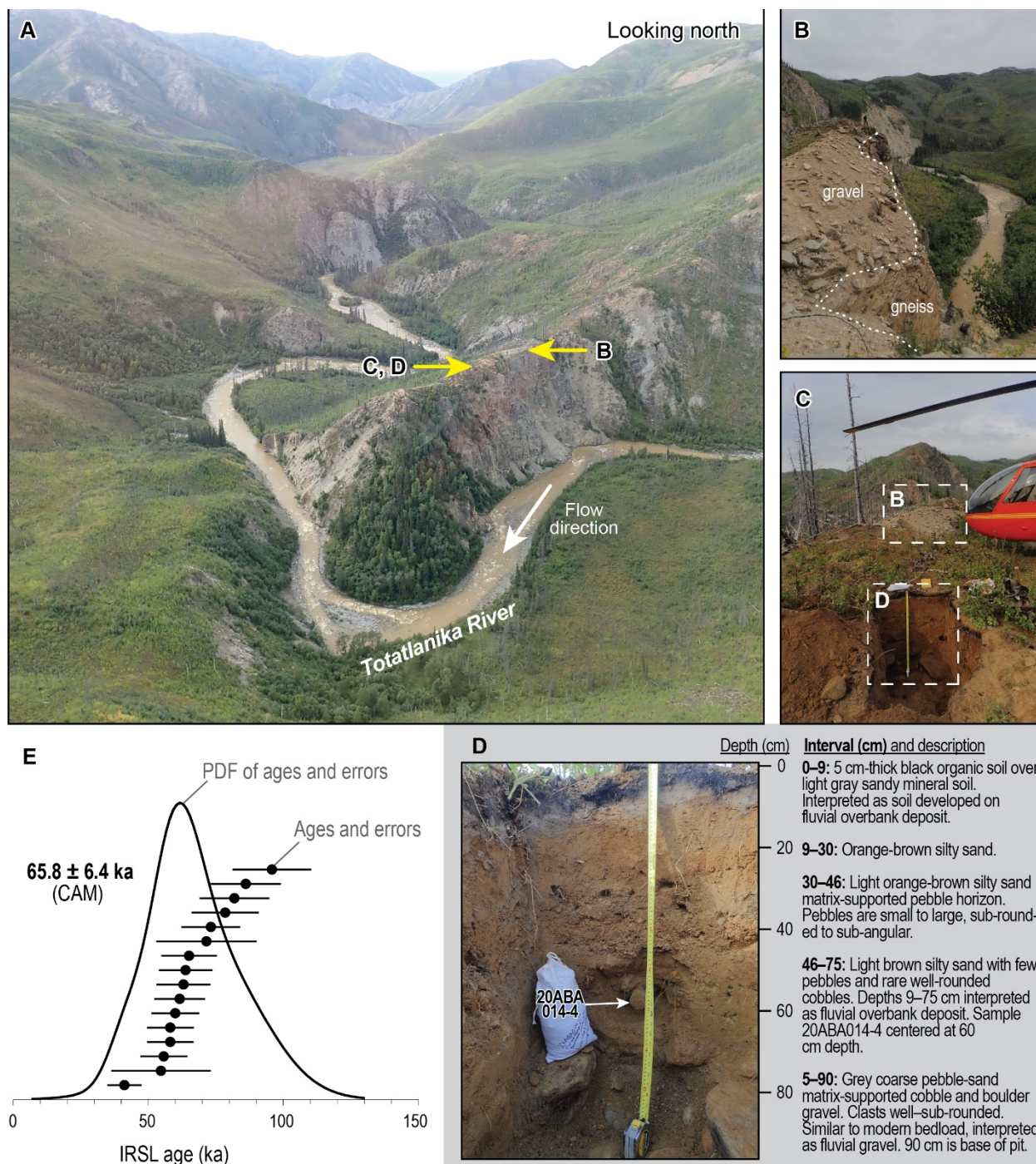


Figure S5: Field site of infrared stimulated luminescence (IRSL) sample 20ABA014-4. (A) Site overview, white dashed line marks strath. Yellow arrows mark (B) gravel-on-strath exposure, (C) sample location (white dashed boxes mark figure panels B and D), and (D) sample pit and description. (E) IRSL ages, probability distribution, and central age model result (CAM; Galbraith & Roberts, 2012) of sample 20ABA014-4.

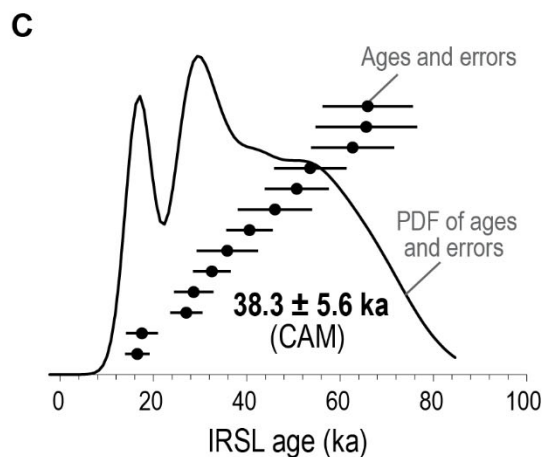
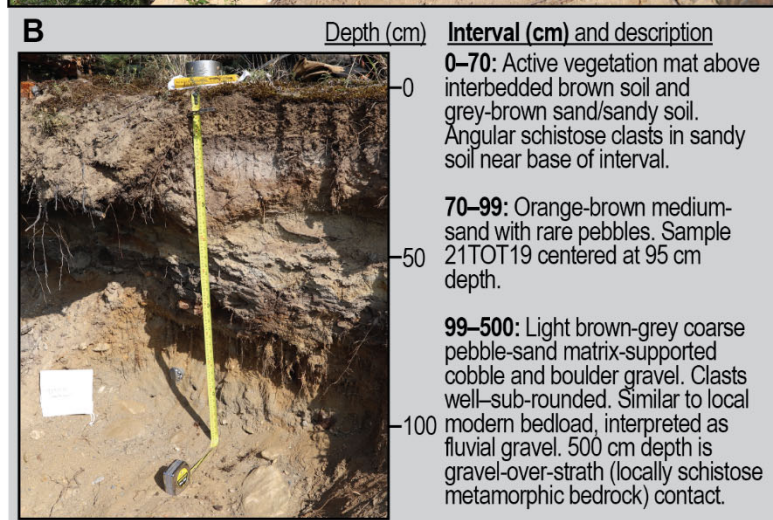
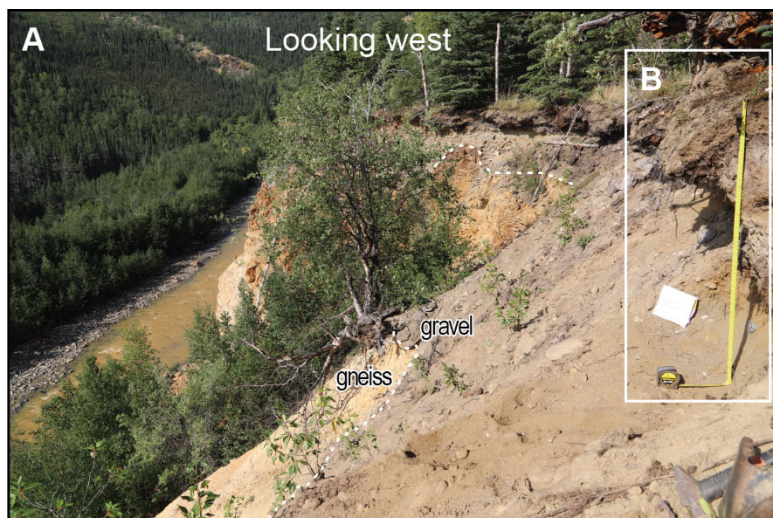


Figure S6: Field site of infrared stimulated luminescence (IRSL) sample 21TOT19. (A) Site overview, Totatlanika River flows into page. White dashed line marks strath, white box marks (B) sample exposure and description. (C) IRSL ages, probability distribution, and central age model result (CAM; Galbraith & Roberts, 2012) of sample 21TOT19.



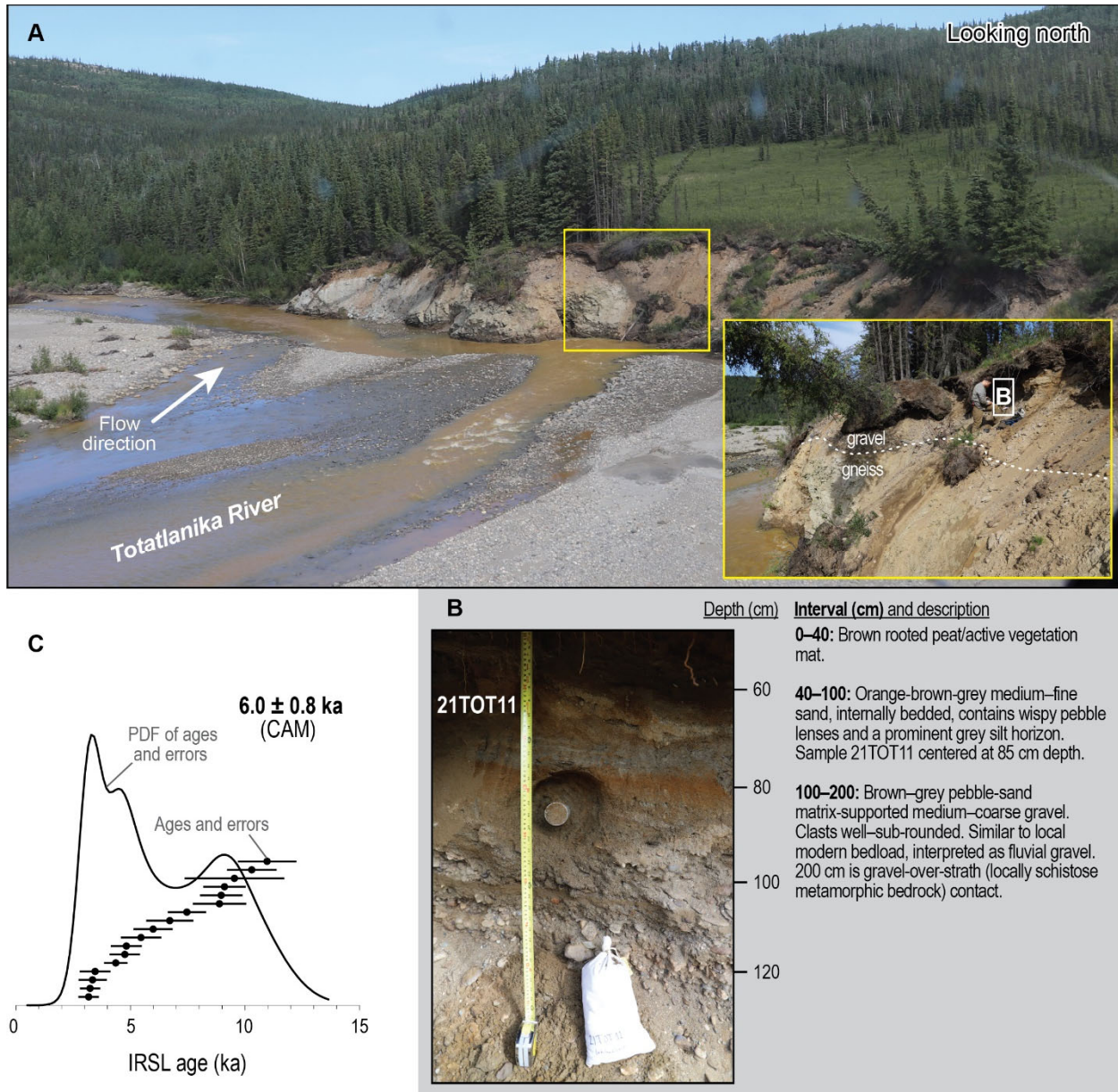


Figure S7: Field site of infrared stimulated luminescence (IRSL) sample 21TOT11. (A) Site overview, yellow box marks inset photo of deposit exposure. White dashed line marks strath, white box marks (B) sample exposure and description. (C) IRSL ages, probability distribution, and central age model result (CAM; Galbraith & Roberts, 2012) of sample 21TOT11.



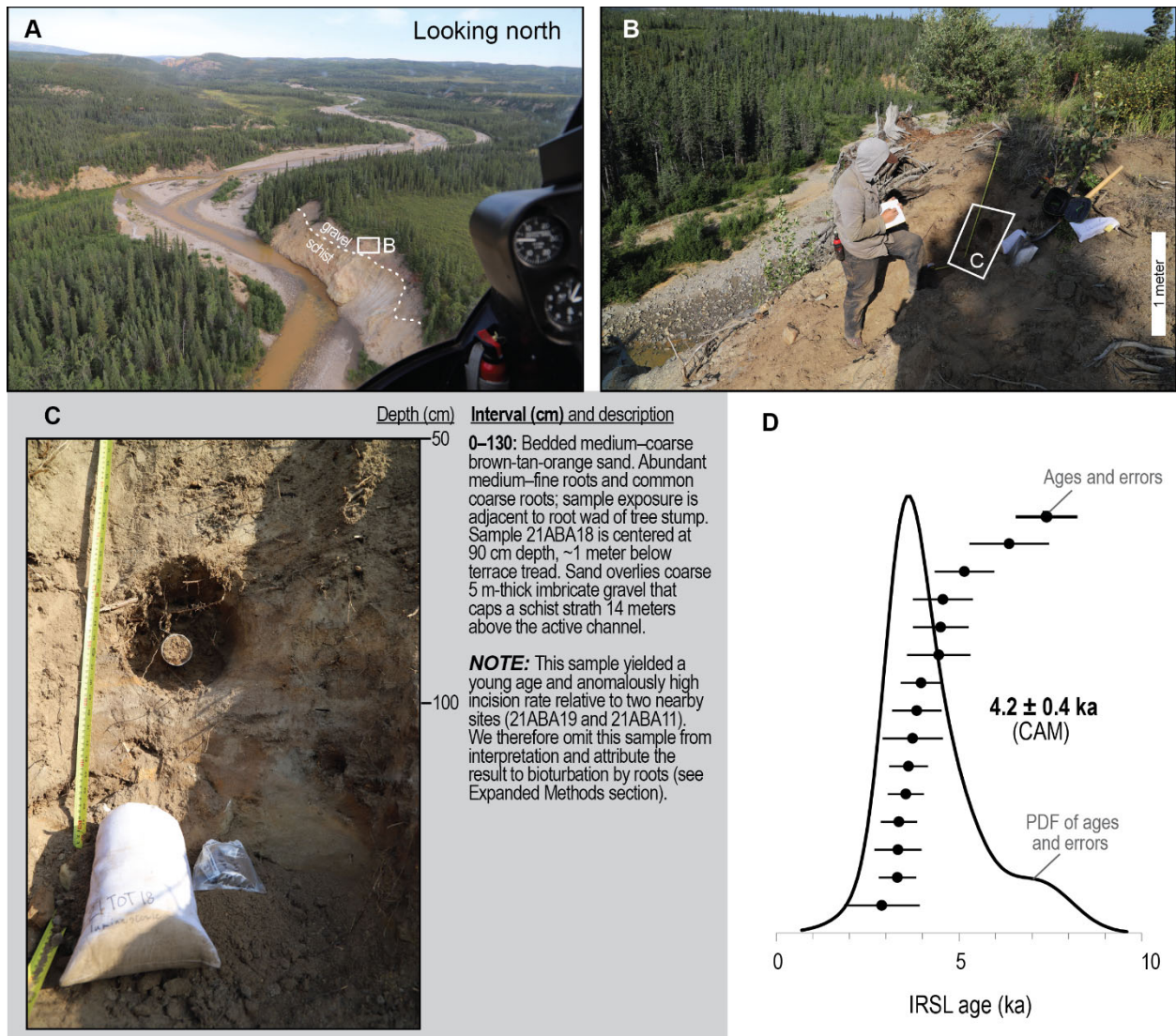


Figure S8: Field site of infrared stimulated luminescence (IRSL) sample 21TOT18. (A) Site overview, white dashed line marks strath, white box marks (B) sample site. White box marks location of (C) sample exposure detail and description. Note prominent roots. (D) IRSL ages, probability distribution, and central age model result (CAM; Galbraith & Roberts, 2012) of sample 21TOT18. This young age implies an anomalously fast incision rate relative to nearby sites 21TOT11 and 21TOT19, and was therefore omitted from interpretation. We attribute the young age to bioturbation by roots (cf. Hanson et al., 2015).

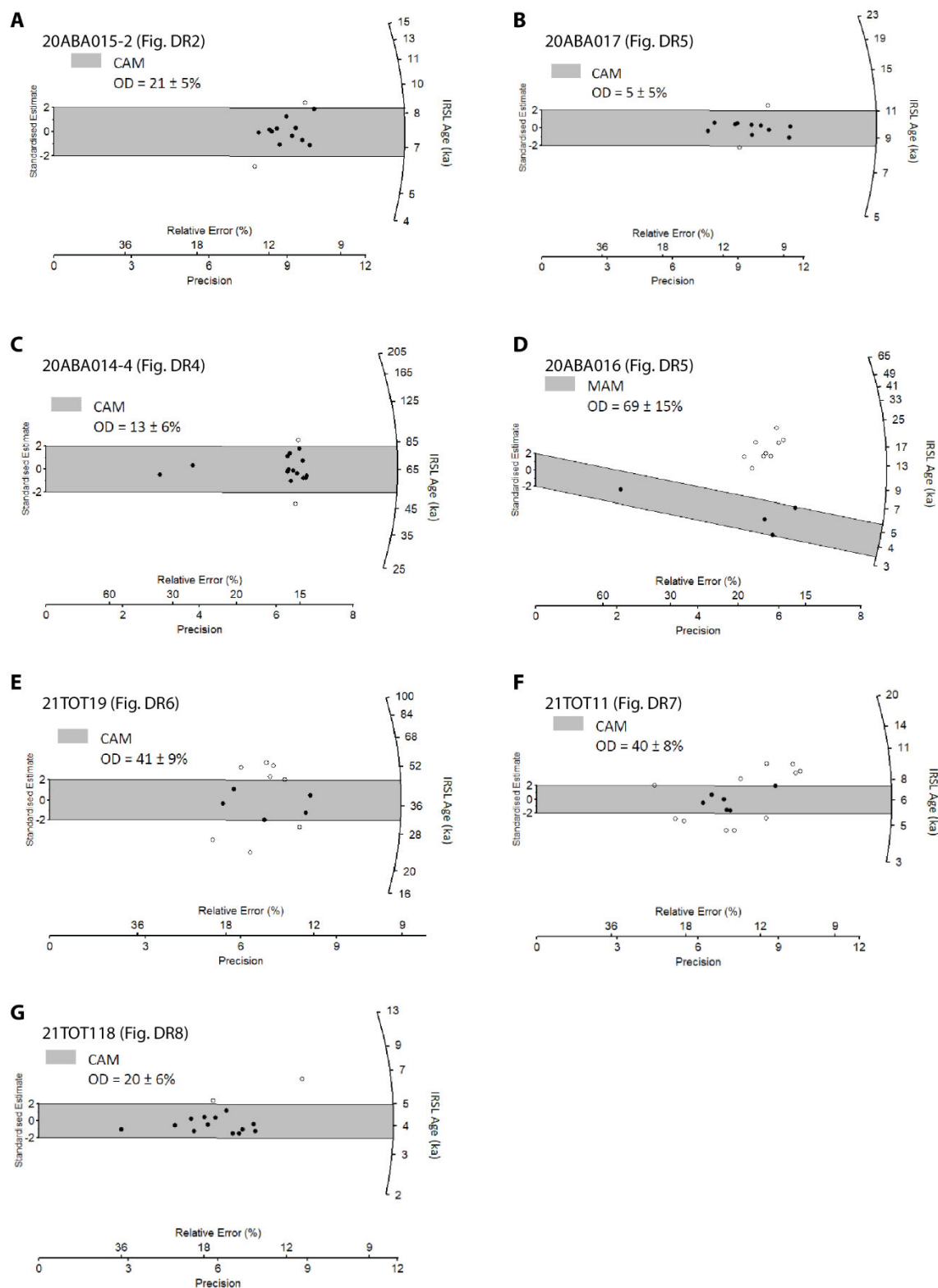


Figure S9: (A–G) Radial plots of infrared stimulated luminescence data. Grey envelopes represent the central age model (CAM) or minimum age model (MAM). Black dots represent aliquot results used for age model, white dots represent aliquot results omitted from age model. OD—overdispersion.